Advanced Energy Conversion Materials
http://ojs.wiserpub.com/index.php/AECM/

UNIVERSAL WISER PUBLISHER

Research Article

Exploring the Interface Between Two Nanoclusters: Insights from Computational Methods

Divya Maldepalli Govindachar, Ganga Periyasamy*

Department of Chemistry, Bangalore University, Bangalore, India
E-mail: ganga.periyasamy@gmail.com

Received: 7 October 2023; **Revised:** 11 December 2023; **Accepted:** 13 December 2023

Abstract: Aggregation of gold nanoclusters (GNCs) with desired properties requires detailed knowledge about the inter-cluster interface and its properties. The stability of $[Au_6]_2$ dimeric cluster configuration has been confirmed based on molecular dynamic simulation at 298 K temperature, 1 atm pressure, and water as solvent. The structural and electronic properties of series of monomeric and dimeric $[Au_6]_2$, $[Au_6H]_2$, $[Au_6CH_3]_2$, $[Au_6C_2H_5]_2$, $[Au_6C_5H_9]_2$, $[Au_6C_6H_{11}]_2$, $[Au_6C_6H_5]_2$, $[Au_6C_6H_4CH_3]_2$, $[Au_6C_6H_4CH_3]_2$, $[Au_6C_2H]_2$, $[Au_6C_2CH_3]_2$ and $[Au_6C_2C_6H_5]_2$ clusters were studied using three different functionals in density functional theoretical methods by considering three different interfaces. The dimerization was found to alter the highest occupied molecular orbital-lowest unoccupied molecular orbital (HOMO-LUMO) gap depending upon the interface between the clusters. The computation predicts that the presence of ligand-ligand (ML-LM) and ligand-metal (ML-ML) interfaces in ligated cluster dimers were found to decrease the HOMO-LUMO gap while the metal-metal (LM-ML) interface leads to larger cluster formations. The change in electronic structures is found to be the reflection of symmetry in the eigenfunctions. The vertical plane of symmetry at the ML-LM interface leads to a smaller HOMO-LUMO gap as a result of degenerate orbitals between the monomeric units. The distortion from the reflection symmetry at the ML-ML interface removes the degeneracy by splitting the orbitals which increases the HOMO-LUMO gap in the ligated clusters. Among the studied ligated nanoclusters, experimentally realized $[Au_6C_2C_6H_5]_2$ possesses a small HOMO-LUMO gap. All the interfaces are found to behave similarly in the presence of various uniform electric fields. The consequences of HOMO-LUMO gaps were observed in redox parameters, and absorption properties and have been explained using molecular orbital plots.

Graphical Abstract:

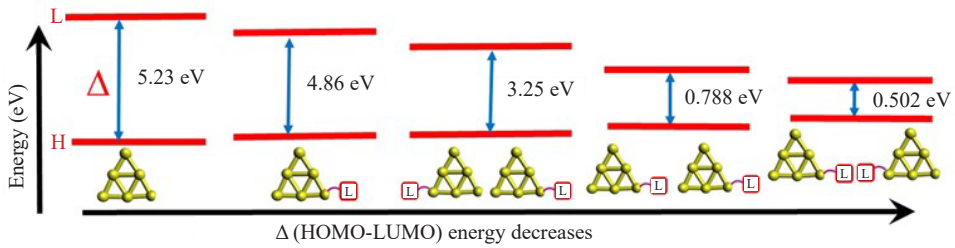

DOI: https://doi.org/10.37256/aecm.5120243746

***Keywords*:** nanoclusters, HOMO-LUMO gap, aggregations, Interactions, dimerization, interface, orientations, self-assembly

1. Introduction

"Interface" refers to the region where the surfaces of the two clusters meet and interact [1-6]. This interface can significantly impact the properties and behavior of the nanoclusters, such as their stability, size, shape, and electronic structure [2-8]. Interactions at the interface can also affect the properties of the individual clusters, such as their electronic and optical properties [9-11]. Creating an interface between two clusters makes it possible to stabilize the structure compared to individual units [12-15]. It can also facilitate the dimerization of metal nanoclusters, forming new configurations with unique electronic, optical, catalytic, and redox properties [16-21]. By making the different interfaces between nanoclusters, it is possible to generate properties that do not exist in either of the individual clusters [7, 9, 22, 23]. Carefully controlling the orientations, and types of the interface, and understanding of the chemical nature of the interface between two nanoclusters lead scientists to design and synthesize new materials with tailored properties for various applications [24-27]. Researchers are using computational methods to explore and understand the interface at the atomic and molecular level, providing insights into the interactions and behavior of the nanoclusters [28-31].

Gold nanoclusters [32] are widely used with ligation and solvation environments for biological [12], optical [30], catalytic [13], and sensing applications [33, 34]. Hence, the integration of building blocks of gold nanoclusters with desired electronic, electrochemical, and magnetic properties into bulk materials become highly challenging for an experimentalist to realize their application due to the possibility of numerous interfaces [17, 35-38]. Further, the microstructural features of the GNCs are key designing factors in self-assembly that control the macroscopic properties such as hardness, toughness, ductility, corrosion, etching, transport, light reflection, scattering, catalysis, sensing, and drug delivery [28, 29, 39-41]. The right geometric configuration of the GNCs at the nanoscale is crucial to designing these materials that require detailed knowledge about the fundamental structure-property relationship [42-45]. The influence of van der Waals interaction between the neighboring clusters towards the chiro-optical properties of the dimeric gold bipyramid plasmonic nanoparticles has been studied using advanced spectroscopic and thermal imaging techniques [43, 44]. The effect of neighboring cluster orientation towards the bulk properties proves to be important for their stability [46-50]. The interface is found to exist either through metal or ligand channels. For example, versatile alkynyl ligands were used by Gorman et al. as the triple bond of an alkynyl ligand coordinates to metal centers in σ or/and π modes [51-54].

Au_6 clusters have been chosen in order to study the various channels of the interface. Au_6 is a known two-dimensional experimentally realized nanocluster with a pyramidal geometry in all three oxidation states and various ligated forms [30, 55]. Earlier work on these clusters provides evidence that the ligation can tune the electronic, electrochemical, and optical properties by passivating the cluster or by integrating it with a metal core [3, 56]. The passivation can occur via a wide range of ligands without disturbing the structure of the metal, which has been studied to a larger extent by various research groups [21, 57-60]. The passivated cluster can come near to each other in various orientation that opens upon various possible non-covalent channel. Herein, the non-polar ligand models have been used in order to understand their effect on nanocluster structure and properties. Further, this work aims to understand the various possible non-covalent interactions of the various size non-polar ligands such as hydrogen, alkyl group, cyclic, and aromatic groups. Moreover, the studies will address the influence of interface on various electronic, electrochemical, and optical properties.

2. Computational method

The dimeric form of various [Au_6] dimers was generated for density functional theory (DFT) computation using molecular dynamics. Three interfaces were generated as in Figure 1, which are ML-LM (Ligand-Ligand, Orientation-I), LM-LM (Metal-Ligand, Orientation-II), and LM-ML (Metal-Metal-Orientation-III). The AMBER99 force fields [61] are used to model the neutral metal atoms which are modeled as lennard-jones (LJ) particles. The LJ parameters

are taken from the literature for gold atoms [62]. These parameters are already used to study the interaction between ligand and metal clusters, which shows the reliability of the parameters. The transferable intermolecular potential three-point (TIP3P) model is considered for water solvents. The molecular dynamics (MD) simulation is performed using the GROMACS-5.1.1 MD package [63] in an initial cubic water box of length 10 Å at room temperature (298 K) and constant atmospheric pressure (1 atm). Initially, the high-energy contacts between the monomers in the initial conformations are removed by minimizing the energy using the steepest decent method. Following that, NPT and NVT simulations are carried out using a leap-frog algorithm for integrating Newton's equation of motion for 1.0 ns at constant temperature and pressure. The periodic boundary condition is applied in all three directions. Electrostatic interactions are calculated with the particle mesh ewald (PME) method. The time step for the MD simulation is 1.5 fs. Atomic coordinates are recorded for every 7.5 ps for trajectory analysis. The final geometry obtained from the simulation was used for the DFT computation.

The DFT calculations are carried out with CAM-B3LYP long-range, wB97XD, and M06-HF dispersion corrected functional, LANL2DZ pseudopotential for Au, and 6-31 + G(d) basis set for all other atoms. Natural charges have been calculated using Natural charge analysis to check the charge distribution in the dimer. All the geometries were considered the lowest energy by performing a scan along with the coordinates method (Coordinates are given in Appendix). The basis set superposition error (BSSE) in interaction energy value is attuned using the Boys and Bernardi counterpoise correction method as set in the Gaussian 09 package [64]. Time-dependent density functional theory has been calculated using the same level of theory for all the aggregations. All minimized dimer models were studied in a uniform electric field (-F) of different strengths were applied and the HOMO-LUMO energy gaps were monitored. The artifact of functional and basis sets has been taken care of by computing the electronic parameters at three different functional and 6-31 + g(d) basis sets using the Gaussian 09 package [64]. All methods were found to show a similar trend, hence the CAM-B3LYP results are used for the discussion below (Table S2).

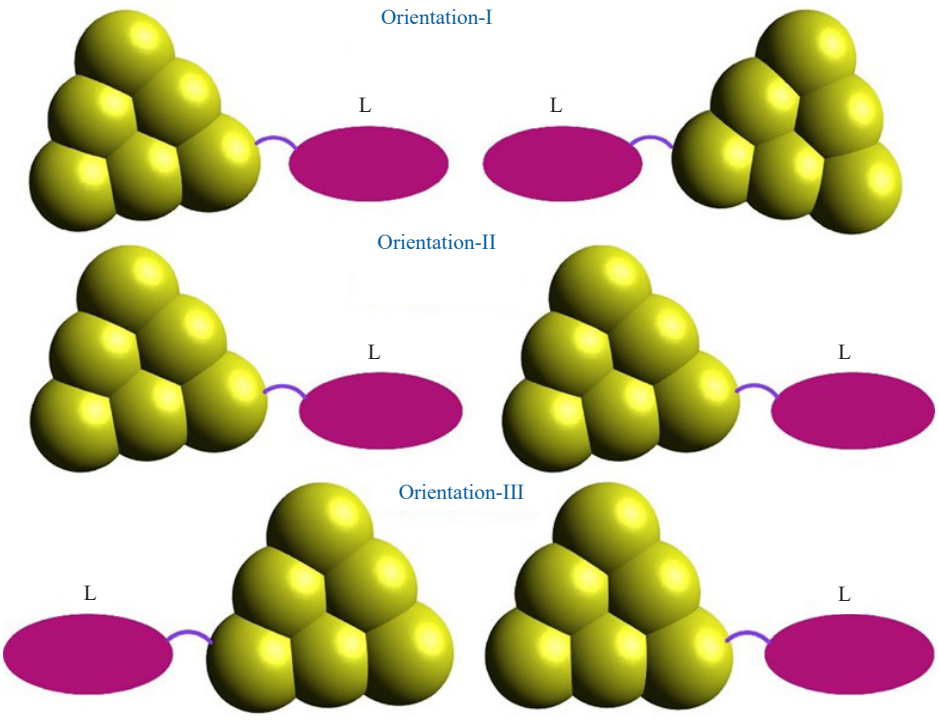

Figure 1. Schematic representation of all the orientations of dimer (monomer [Au_6L]-monomer [Au_6L]) interactions studied, where L = H, CH_4, C_2H_6, C_5H_{10}, C_6H_{12}, C_6H_6, C_7H_8, C_2H_2, C_2HCH_3 and $C_2HC_6H_6$

The vertical ionization potential (VIP), vertical electron affinity (VEA), dimers interaction energies (DIE) are calculated using the equations given below.

$$VIP = E_{(N+1)\text{ (cation at optimized neutral geometry)}} - E_{(N)\text{ (optimized neutral)}}$$

$$VEA = E_{(N)\text{ (optimized neutral)}} - E_{(N-1)\text{ (anion at optimized neutral geometry)}}$$

Basis set superimposition error (BSSE) corrections are carried out using the Boys and Bernardi counterpoise correction method as implemented in the Gaussian 09 package at the same level of theory using the equation,

$$IE = [E_{(dimer)} - (E_{(monomer1)} + E_{(monomer2)})] + BSSE.$$

Charging energy (U_c) is calculated using the formula, [57]

$$U_C = VEA + VIP = E_{(N+1)} - 2E_{(N)} + E_{(N-1)}.$$

3. Result and discussion

$[Au_6]_2$ dimeric clusters have been considered for MD simulation to study the structural integrity of the cluster. The computed root mean square deviation (RMSD) data in Figure 2 provides evidence for the minimal change in the structure from the initial coordinates that show the stability of the clusters. Further, the computed energy plot shows at 20 ps of NPT and NVT simulations, the dimeric structure reached the equilibrium. The MD simulations only support the structural integrity for two monomeric units for the longer time scales. Hence, the electronic structure and its properties were studied using the DFT methods.

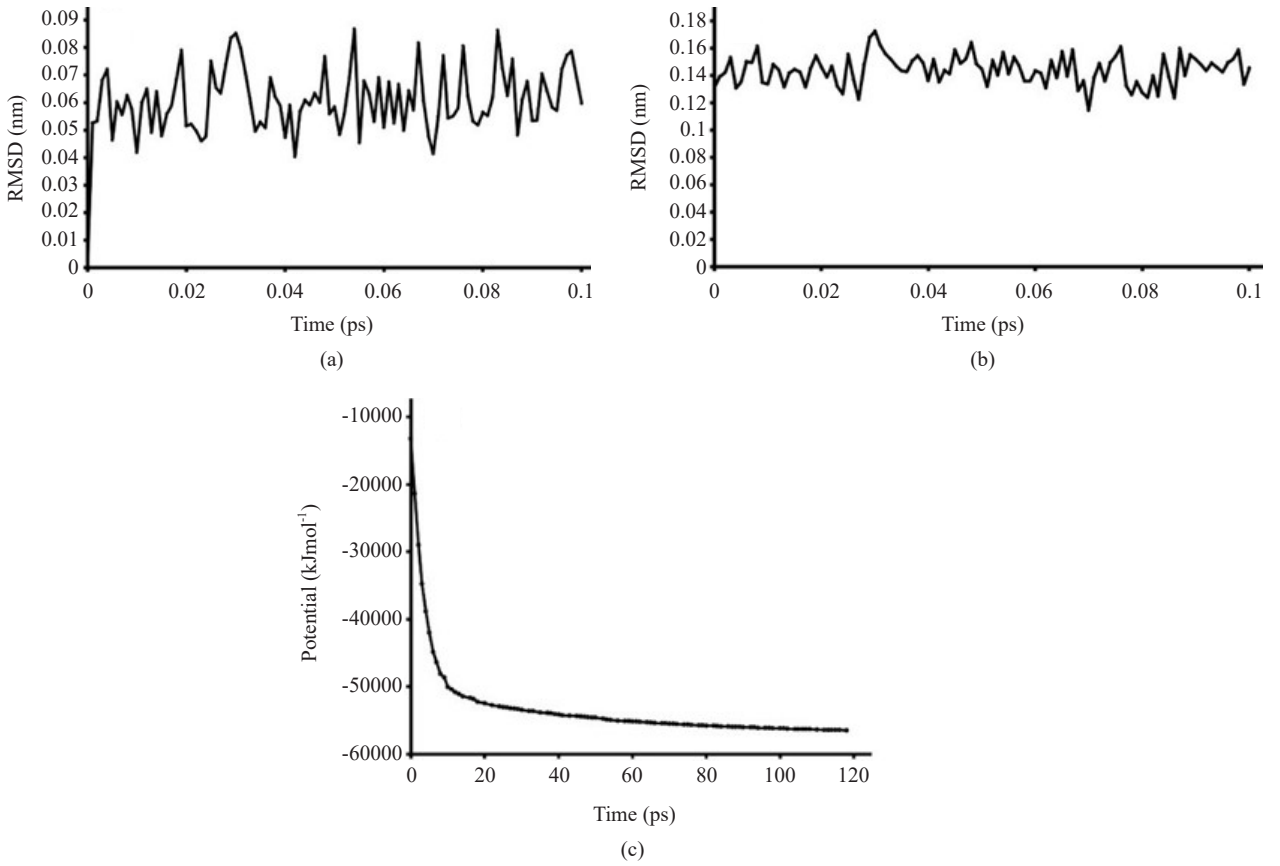

Figure 2. RMSD plot relative to the energy minimized structure after 1 ns (a) NVT and (b) NPT simulation (c) Potential energy plot of energy minimization for 1 ns

Table 1. Computed BSSE corrected binding energy (in kcal mol^{-1}) for singlet and triplet spin states for the orientation 1 at CAMB3LYP level theory for all ligated dimeric clusters

Au_6-dimer	Δ (Triplet)		Δ (singlet)	BE	
	α	β		Singlet	Triplet
$[Au_6]_2$	-	-	4.21	-6.81	2.12
$[Au_6H]_2$	3.082	2.625	4.357	-33.07	7.55
$[Au_6CH_3]_2$	4.596	4.145	1.569	-4.44	3.01
$[Au_6C_2H_5]_2$	5.244	4.176	1.005	-42.60	2.66
$[Au_6C_5H_9]_2$	4.924	4.306	0.787	-44.01	11.89
$[Au_6C_6H_{11}]_2$	4.659	4.517	0.637	-34.13	0.86
$[Au_6C_6H_5]_2$	4.851	4.275	0.578	-34.45	-1.68
$[Au_6C_6H_4CH_3]_2$	4.833	4.292	0.502	-35.15	-1.82
$[Au_6C_2H]_2$	5.004	2.649	0.794	-33.79	4.11
$[Au_6C_2CH_3]_2$	4.966	2.654	0.762	-36.23	-4.42
$[Au_6C_2C_6H_5]_2$	4.621	2.704	0.533	-42.63	-8.24

We have calculated the attractive and repulsive force between the dimers as a function of inter-cluster distance (Figure 3). We have stabilized the dimeric clusters in the singlet and triplet spin states.

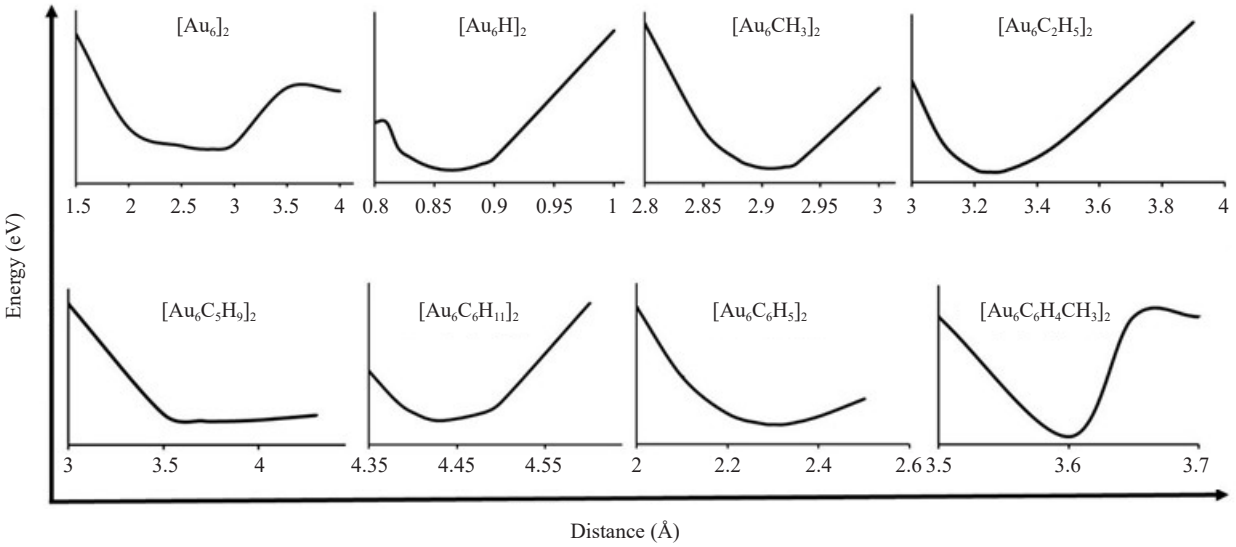

Figure 3. The relative electronic energy with respect to inter cluster distance for all the geometries studies for orientation I

The singlet state refers to a state where the total spin of the electrons in the dimeric system is zero, while the triplet state refers to a state where the total spin is one. The singlet state is more stable with negative binding energy, while the

triplet state has positive binding energy (Table 1). The lesser stability of triplet states might be the effect of spin pairing and the strength of the exchange interaction between the two monomers. The $[Au_6]_2$ dimeric bare clusters show the equilibrium inter-cluster distances of 2.8 Å at the singlet state (Figure 4).

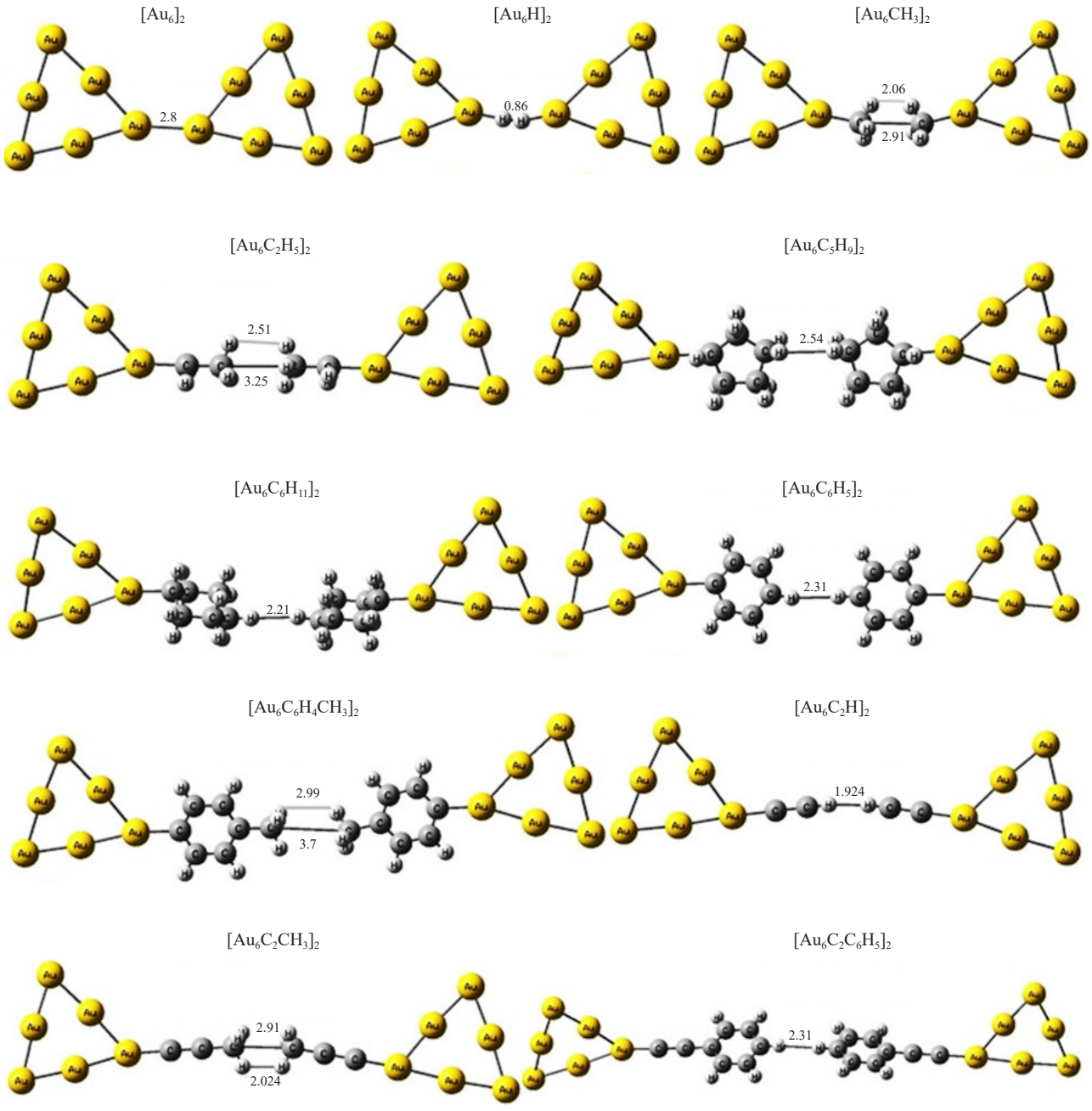

Figure 4. Computed lowest energy geometries of all the ligated cluster of orientation I at CAMB3LYP level theory, inter-cluster distances are given in Å

The ligation leads to three orientations: I, II, and III. In orientations I and II, ligand-ligand and ligand-metal interfaces exist with an inter-nuclear distance of 1.6 to 2.1 Å. At the same time, the optimization of orientation-III leads to a cluster with $[Au_{12}L_2]$ unit in all ligated forms. The interaction and interaction distance of dimer $[Au_6C_6H_5]_2$ are given in Figure 5 to show the stability of different orientations. Similar studies have been carried out for the other

ligated clusters of $[Au_6H]_2$, $[Au_6CH_3]_2$, $[Au_6C_2H_5]_2$, $[Au_6C_5H_9]_2$, $[Au_6C_6H_{11}]_2$, $[Au_6C_6H_5]_2$, $[Au_6C_6H_4CH_3]_2$, $[Au_6C_2H]_2$, $[Au_6C_2CH_3]_2$ and $[Au_6C_2C_6H_5]_2$ in three different orientations. We have observed a comparable pattern in all the chosen models, and the inter-cluster distance given in Figures 3 and 4, is found to follow the same trend. The van der Waals interaction dominates the interface, where the inter-cluster distances are proportional to ligand size, shape, and the electron cloud's polarizability. Herein, the distance between clusters is typically minimal, leading to a significant increase in interactions reflected in binding energy.

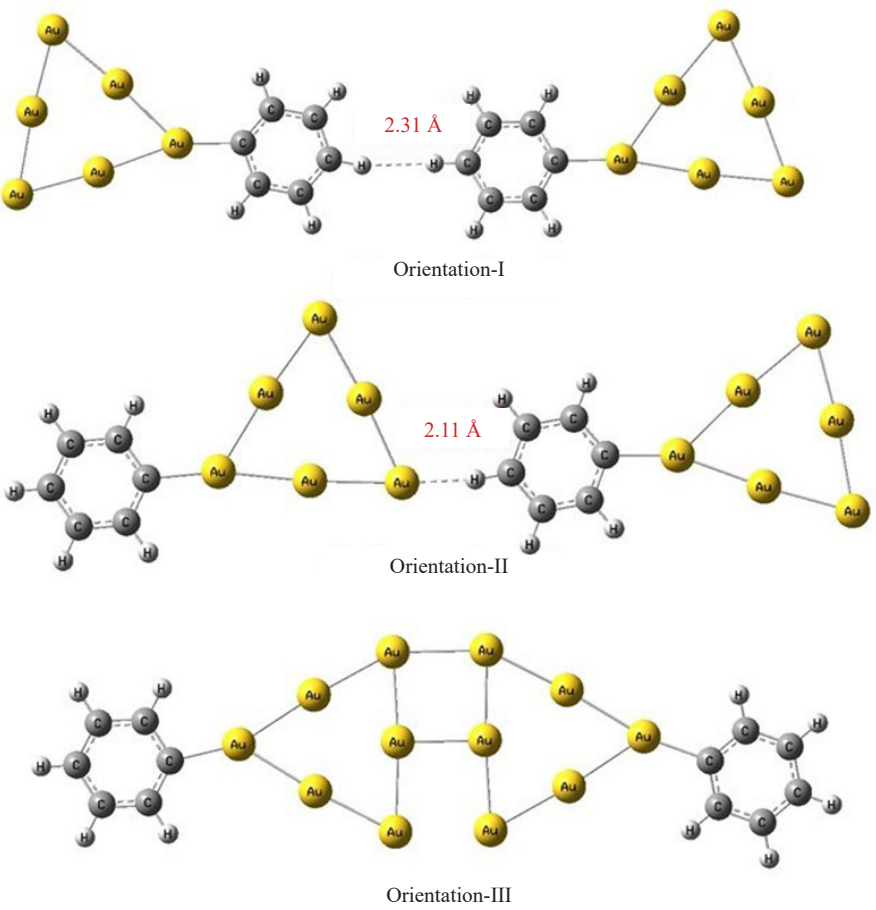

Figure 5. Optimized geometry of different orientations of $[Au_6C_6H_5]_2$ models. Note that orientation-III leads to the $Au_{12}(C_6H_5)_2$

The computed negative binding energies show the larger stabilization of the cluster in the monomer-ligated form (Table 1). Among the clusters $[Au_6C_2C_6H_5]_2$ has the highest negative values with larger binding affinity, and others exist in the following order $[Au_6C_2C_6H_5]_2$ > $[Au_6C_5H_9]_2$ > $[Au_6C_2H_5]_2$ > $[Au_6C_2CH_3]_2$ > $[Au_6C_6H_4CH_3]_2$ > $[Au_6C_6H_5]_2$ > $[Au_6C_6H_{11}]_2$ > $[Au_6C_2H]_2$ > $[Au_6H]_2$ > $[Au_6]_2$ > $[Au_6CH_3]_2$. The molecular electrostatic potential maps simulated to understand the types of interactions between the clusters in all three orientations of $[Au_6C_2C_6H_5]_2$ and $[Au_6C_6H_5]_2$ as shown in Figure 6; The MEP plots exhibit a symmetric pattern, wherein ML-LM displays vertical reflection symmetry, a feature absent in the other two orientations. The three interfaces demonstrate distinct distribution patterns:

(i) Orientation I, molecular electrostatic potential (MEP) plot shows a symmetric charge distribution, where both monomers have the same charge distribution pattern.

(ii) In Orientation II, the charge is wholly delocalized over the entire system.

(iii) In orientation III, the dipole is generated as in a ligated monomeric cluster, where the positive polarization is at the central metal cluster and the ligands are negatively polarized at the terminal. The delocalization at the interface

provide evidence for the formation of a larger cluster via chemical bond.

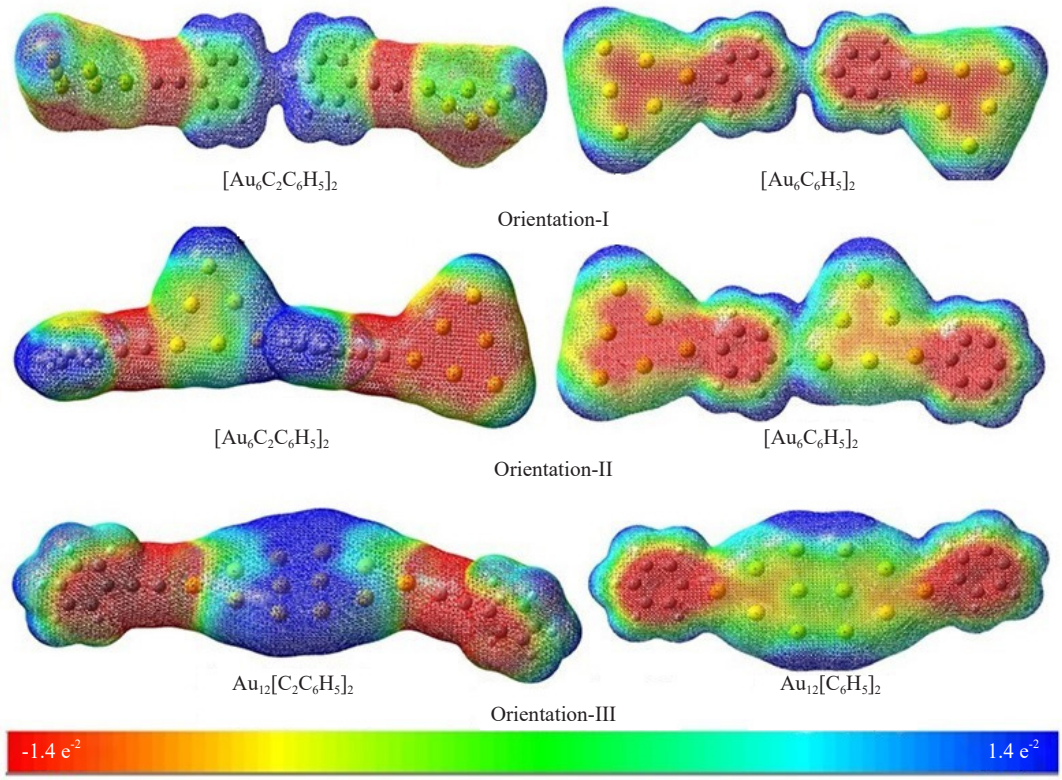

Figure 6. The molecular electrostatic potential for $[Au_6C_2C_6H_5]_2$ and $[Au_6C_6H_5]_2$ models in all three orientations

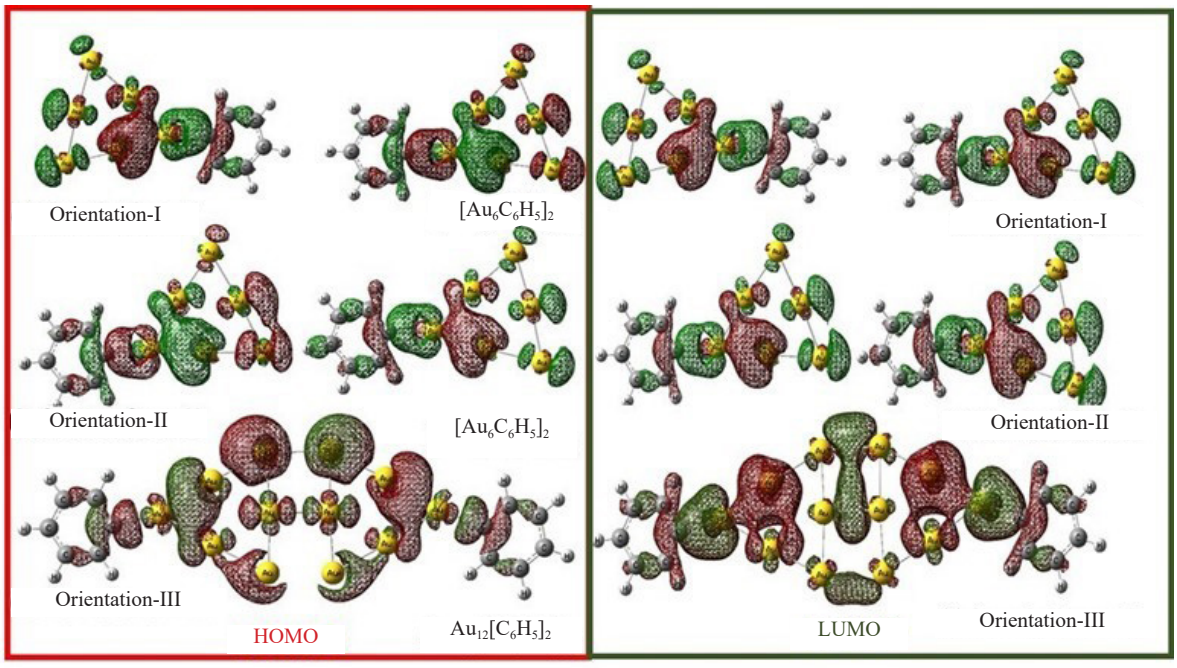

Figure 7. Orbital plots of all the dimers $[Au_6C_2H_5]_2$ in three different orientations plotted at the CAM-B3LYP level with an isocontour value of 0.02 $Å^{-3}$

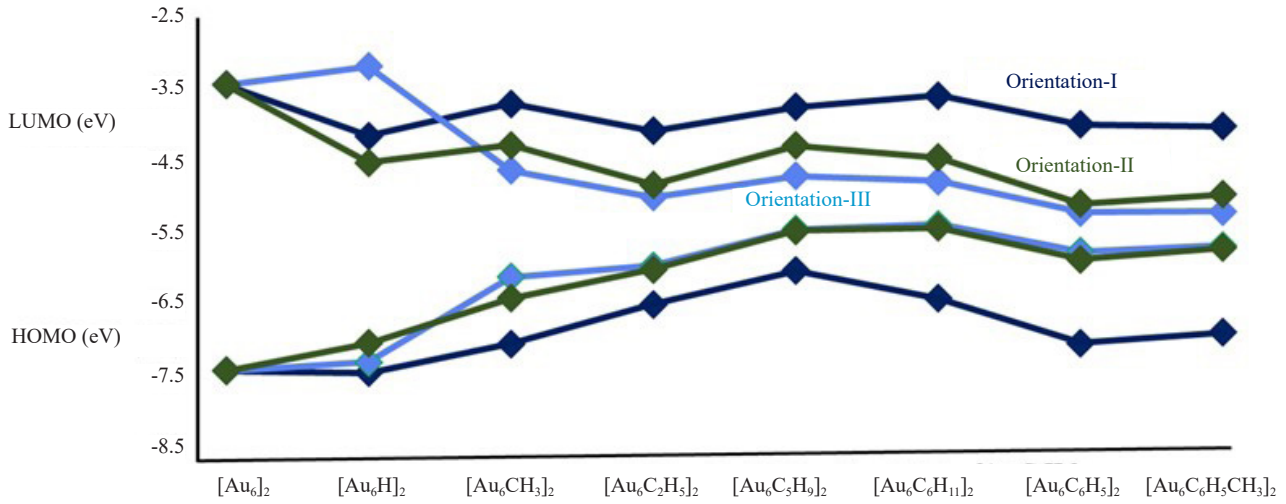

Figure 8. Computed HOMO and LUMO energies in eV plotted for orientation I, orientation II, and orientation III

Table 2. Computed $E_{(HOMO)}$, $E_{(LUMO)}$, Δ(HOMO-LUMO), VEA, VIP and electronic properties, charging energy U_c as VEA + VIP = $E_{(N+1)} - 2E_{(N)} + E_{(N-1)}$ in eV and λ_{max} in nm of various ligated dimers at CAMB3LYP theory for orientations I and II and Alkynyl ligated dimers (in Bold font [48-51])

Models		$E_{(HOMO)}$	$E_{(LUMO)}$	Δ (eV)	VEA	VIP	U_c (eV)	λ_{max} (nm)
$[Au_6]_2$		-7.515	-3.305	4.21	3.025	-7.786	4.761	496
$[Au_6H]_2$	I	-7.389	-3.032	4.357	2.731	-7.636	4.905	462
	II	-7.110	-4.447	2.663	2.812	-7.421	4.609	565
$[Au_6CH_3]_2$	I	-6.134	-4.565	1.569	4.297	-6.411	2.114	1,086
	II	-6.445	-4.193	2.252	4.321	-5.878	1.557	1,176
$[Au_6C_2H_5]_2$	I	-5.964	-4.959	1.005	4.847	-6.074	1.227	952
	II	-6.023	-4.774	1.249	5.216	-6.457	1.241	1,012
$[Au_6C_5H_9]_2$	I	-5.434	-4.647	0.787	4.705	-5.652	0.947	5,612
	II	-5.455	-4.202	1.253	4.122	-4.989	0.867	6,357
$[Au_6C_6H_{11}]_2$	I	-5.361	-4.723	0.637	4.500	-5.671	1.171	7,600
	II	-5.404	-4.377	1.027	4.763	-5.788	1.025	8,012
$[Au_6C_6H_5]_2$	I	-5.757	-5.179	0.578	4.895	-6.064	1.169	14,122
	II	-5.875	-5.051	0.824	5.231	-6.121	0.890	15,014
$[Au_6C_6H_4CH_3]_2$	I	-5.669	-5.167	0.502	4.902	-5.888	0.986	23,295
	II	-5.702	-4.914	0.788	4.895	-5.723	0.828	22,123
$[Au_6C_2H]_2$	I	-6.748	-5.954	0.794	5.907	-6.064	0.156	17,211
	II	-6.568	-5.731	0.807	5.612	-5.981	0.369	18,321
$[Au_6C_2CH_3]_2$	I	-6.600	-5.838	0.762	5.855	-5.824	0.031	16,685
	II	-6.654	-5.723	0.931	5.642	-5.762	0.120	16,754
$[Au_6C_2C_6H_5]_2$	I	-6.428	-5.895	0.533	5.864	-5.657	0.206	18,665
	II	-6.571	-5.678	0.893	5.324	-5.581	0.257	19,012

Moreover, the computed dipole moment analysis shows that ligated clusters are more polarized than bare clusters, and the dipole moment points towards the ligand plane (Table S1). The order of polarization for the ligated dimeric nanoclusters follows alkane ligated < aromatic ligated < cycloalkane ligated, and concerning orientation follows orientation II > orientation I > orientation III (Table 1). The more significant polarization in the charges at the computed orientations II and I is due to the distortion in reflection symmetry between the monomeric clusters in dimeric form (Figure 1).

We have plotted and analyzed the fermi-level molecular orbitals to understand the charge distribution pattern. Irrespective of orientations, the computed eigenfunctions in Figure 7 show the significant contribution of ligands and metal at the fermi level (HOMO and LUMO). This provides evidence for the charge polarization at the dimeric cluster, as observed in the ligated monomeric cluster. The ligand 2p and gold 3d orbitals were found to be dominant at the HOMO and LUMO (Figures S1 in Appendix). The overlapping between the atomic orbitals leads to a dominant σ-bond between ligands and metal clusters in all models except in the alkynyl ligand-coordinated ML-ML and ML-LM dimers. The alkynyl group shows the π bonding modes (with back bonding features). Note that the σ, π, and extended conjugation were found to support the decrease in HOMO-LUMO gaps (Figure S1 and Table 2 and Table S3 in Appendix) in orientations I and II.

Moreover, the symmetry of the ligand was also found to play a role as a higher rigid (aromatic ring) containing $[Au_6C_6H_4CH_3]_2$, $[Au_6C_2C_6H_5]_2$, and $[Au_6C_6H_5]_2$ models having lower HOMO-LUMO gap. The computed eigenvalues in Figure 8 show that in orientations I and II, LUMO orbitals are more stabilized than in orientation III owing to the delocalization of electron density distribution. The eigenfunctions of HOMO and LUMO have similar distribution patterns, and the gap occurs due to the dimer's symmetry breaking. In Figure 8 and Table 2, we have given the computed HOMO-LUMO gaps (Δ) for all three orientations. Orientations I and II were found to decrease the Δ values, while orientation III showed a similar trend as monomeric ligated clusters. The degeneracy between the orbitals of monomeric units was apparent from the HOMO-LUMO plots of LM-ML interface clusters. Hence the $[Au_{12}L_2]$ and $[Au_6L_2]$ were found to follow a similar trend in the properties. The polarization of the ligand triggers the stabilization and destabilization factors when compared to bare $[Au_6]_2$ dimers. Among the model studied here the $[Au_6C_6H_4CH_3]_2$ $[Au_6C_2C_6H_5]_2$ and $[Au_6C_6H_5]_2$ models have the lowest Δ values of 0.502, 0.533, and 0.578 eV, respectively. The effect of functional in the HOMO-LUMO gaps was analyzed by choosing wB97XD and M06HF functional, which follow the same trend as CAM-B3LYP (Figure 9 and Table S2 in Appendix).

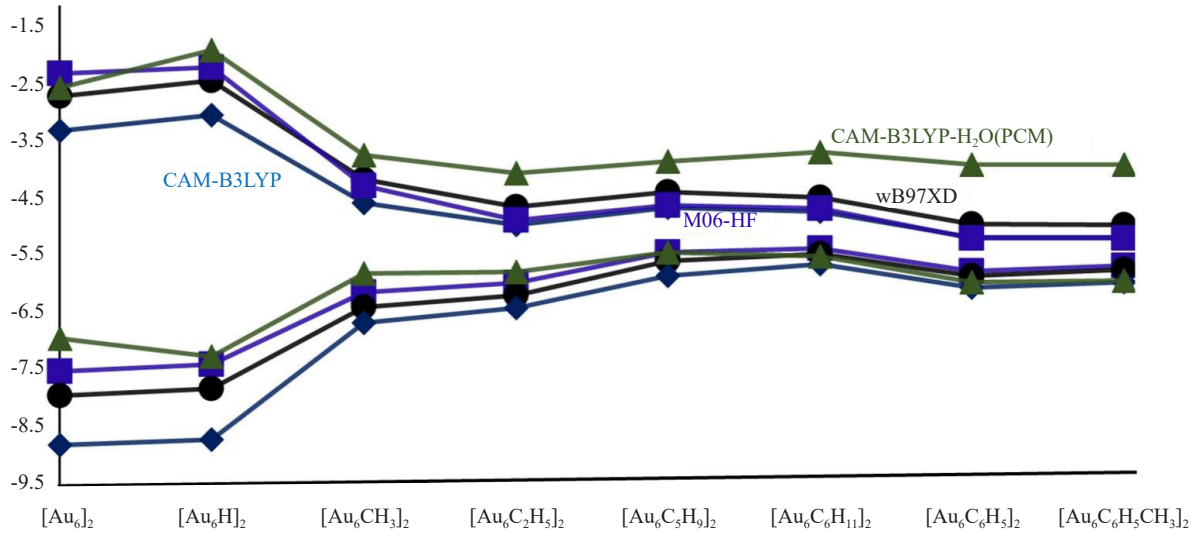

Figure 9. Computed HOMO and LUMO energies in eV plotted for all the aggregations studied with the Functional CAM-B3LYP, CAM-B3LYP (PCM, H_20), wB97XD, M06-HF

Further, we have considered the implicit solvent media to understand the effect of solvent for orientation I. The

water dielectric medium destabilizes the LUMO; as a result, the Δ value increased by 1.5 eV on $[Au_6C_6H_4CH_3]_2$, $[Au_6C_2C_6H_5]_2$, and $[Au_6C_6H_5]_2$ models (Table S2 in Appendix). This strongly suggests the importance of the first neighbor and its orientations. In extension of this, we have introduced the external uniform electric field to see the effect on HOMO and LUMO energies and eigenfunctions. The polarization effects of an electric field are shown by the increasing dipole moments and charge localization on the gold clusters with an increase in field strength (Table 3). The presence of a uniform electric field does not alter the eigenvalues and eigenfunctions due to the complete delocalization of charges in the dimer $[Au_6C_2C_6H_5]_2$ and $[Au_6C_6H_5]_2$ (Figure 5).

Table 3. Computed $E_{(HOMO)}$, $E_{(LUMO)}$, Δ(HOMO-LUMO) in eV and Charge of a single unit in the dimer in e for different electric field applied for various ligated dimers in orientation I

Au_6-dimer	Electric field (4×10^{-4})				Electric field (8×10^{-4})				Electric field (1×10^{-3})			
	$E_{(HOMO)}$	$E_{(LUMO)}$	Δ (eV)	Charge	$E_{(HOMO)}$	$E_{(LUMO)}$	Δ (eV)	Charge	$E_{(HOMO)}$	$E_{(LUMO)}$	Δ (eV)	Charge
$[Au_6]_2$	-7.606	-3.397	4.209	0.016	-7.695	-3.491	4.204	0.027	-7.738	-3.538	4.2	0.032
$[Au_6H]_2$	-7.376	-2.999	4.377	0.070	-7.371	-3.003	4.368	0.089	-7.367	-3.006	4.361	0.099
$[Au_6CH_3]_2$	-6.134	-4.563	1.571	0.043	-6.135	-4.561	1.574	0.102	-6.136	-4.560	1.576	0.131
$[Au_6C_2H_5]_2$	-5.957	-4.951	1.006	0.045	-5.948	-4.941	1.007	0.114	-5.943	-4.936	1.007	0.148
$[Au_6C_5H_9]_2$	-5.438	-4.651	0.787	0.119	-5.441	-4.654	0.787	0.201	-5.442	-4.655	0.787	0.242
$[Au_6C_6H_{11}]_2$	-5.356	-4.718	0.638	0.097	-5.352	-4.714	0.638	0.191	-5.351	-4.712	0.639	0.238
$[Au_6C_6H_5]_2$	-5.754	-5.155	0.599	0.102	-5.751	-5.172	0.579	0.200	-5.750	-5.171	0.579	0.249
$[Au_6C_6H_4CH_3]_2$	-5.665	-5.162	0.503	0.115	-5.662	-5.159	0.503	0.224	-5.661	-5.158	0.503	0.279
$[Au_6C_2H]_2$	-6.748	-5.950	0.798	0.079	-6.750	-5.947	0.803	0.162	-6.752	-5.945	0.807	0.202
$[Au_6C_2CH_3]_2$	-6.599	-5.835	0.764	0.018	-6.602	-5.832	0.77	0.107	-6.604	-5.830	0.774	0.151
$[Au_6C_2C_6H_5]_2$	-6.426	-5.892	0.534	0.114	-6.427	-5.887	0.54	0.232	-6.428	-5.884	0.544	0.291

Further, the influence of the electrochemical properties, the charging energies (Uc), were computed by vertically oxidizing and reducing the cluster (Table 2). The computed results show that the addition of electrons requires lower energy than the removal of an electron as a characteristic of the gold clusters. As expected, orientation III follows a similar trend as $[Au_6L]$. Further, the computed charging energy for orientations I and II decreased as the result of interface interactions from bare $[Au_6]$: 4.76 eV to ligated $[Au_6C_6H_4CH_3]_2$: 0.98 eV in the series (Table 2). The ligated clusters $[Au_6C_5H_9]_2$ and $[Au_6C_2CH_3]_2$ in orientations I and II have 0.03 eV which is smaller than the measured Uc of the larger size Au_{55} cluster (0.3-0.5 eV) [57, 65]. This suggests that the orderly arranged smaller cluster can mimic the larger size cluster properties. The electron density difference between the neutral and charged clusters was plotted to understand the influence of ligands in charging and discharging. The complete delocalized electron density pattern shows that the electrons are added and removed from both the units of the metal cluster (Figure 10 and Figure S2 in SI). The larger extent of delocalization might be the reason for the lowering of Uc in orientations I and II.

The absorption wavelength is inversely proportional to the HOMO-LUMO gaps. The delocalized nature of the orbitals results in HOMO to LUMO excitation in all three orientations. The change in Δ value reflected in the red-shift by λmax 450 to 23,300 nm during the ligation (Table 2) of orientations I and II. However, in the orientation-III is found

to have an absorption maximum between 450 to 700 nm.

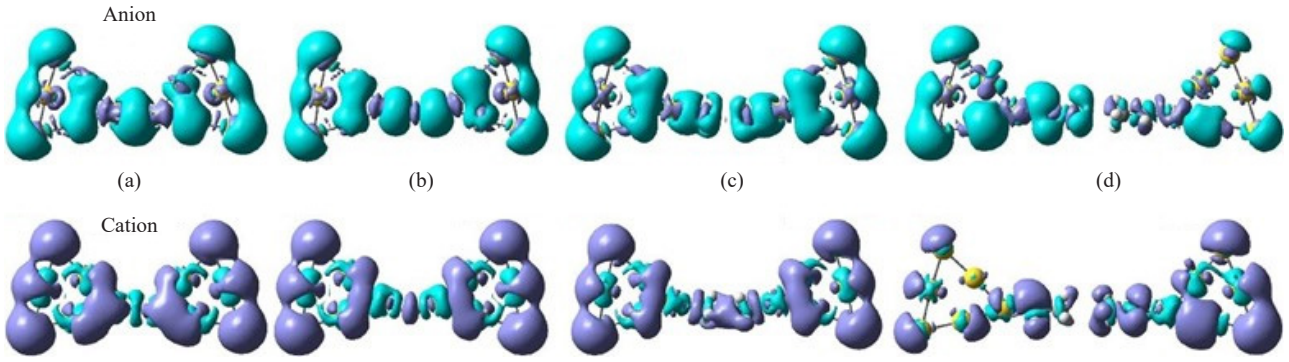

Figure 10. Computed plots of electron density difference between the neutral and charged clusters, where (a) $[Au_6]$ (b) $[Au_6H]_2$, (c) $[Au_6CH_3]_2$, (d) $[Au_6C_2H_5]_2$, plotted with a contour value of 0.02 $Å^{-3}$

4. Conclusion

The work concludes that self-assembly, and interface is a controlling parameter and plays a vital role in tuning the HOMO-LUMO gap. Three dominant interfaces are possible while dimerizing the ligated clusters. The M-M interface leads to the formation of the larger single cluster as in orientation III. The formation of larger clusters shifts the absorption to a larger wavelength, where the ligand plays a major role. The ML-ML and ML-LM interfaces can tune the electronic properties effectively. The computations suggest at the microscopic level, the interface symmetry was found to alter the degeneracy between the monomeric unit which influences the electronic structure of the dimeric unit. The removal of degeneracy decreases the HOMO-LUMO gap by increasing the polarization. Especially, $[Au_6C_6H_4CH_3]_2$ dimeric clusters in ML-ML and ML-LM interface had very low (0.5 eV) HOMO-LUMO gap that consequently makes the Uc smaller which might make them ideal candidates for single electron transistor. Further, the computations show that the smaller-size clusters can also be self-assembled with appropriate orientations to mimic the bulk cluster properties. The interface properties of ligand-protected clusters and the understanding of ligand effects are essential for the control of charge transfer and redox properties in small arrays in view of Nanoelectronics applications.

Supporting information

Computational Methods and software details used in this work, Computed Binding energies, and dipole moments, pictures of lowest energy geometries of orientation I, eigen function plots, HOMO and LUMO energy plots for all orientations models, electron density difference plots. Redox and optical property information. Computed coordinates (DATA) for all the models used in this work are given.

Author contributions

Divya Maldepalli Govindachar: Data Curation, Formal Analysis, Investigation, Visualization, Writing-original draft.

Ganga Periyasamy: Conceptualization, Funding acquisition, Methodology, Project Administration, Resources, Software, Supervision, Validation, Writing-Review & editing.

Acknowledgement

This work is supported by DST-CRG (001606) funded by the Government of India, UGC-FRP (2013-SR-21-FRP), and VGST-KFIST-L2- GRD 1021.

Conflict of interest

The authors declare no competing financial interest.

References

[1] Tang Q, Hu G, Fung V, Jiang DE. Insights into interfaces, stability, electronic properties, and catalytic activities of atomically precise metal nanoclusters from first principles. *Accounts of Chemical Research*. 2018; 51(11): 2793-2802.

[2] Park S, Kim G, Kwon YK. First-principles investigation on dimerization of metal-encapsulated gold nanoclusters. *RSC Advances*. 2014; 4(1): 192-198.

[3] Lo WS, Chou LY, Young AP, Ren C, Goh TW, Williams BP, et al. Probing the Interface between encapsulated nanoparticles and metal-organic frameworks for catalytic selectivity control. *Chemistry of Materials*. 2021; 33(6): 1946-1953.

[4] Sun J, Sun F, Tang J, Tang X, Wu Q, Huo R, et al. Carboxylate engineering for manipulating the optical and assembly properties of copper clusters. *Inorganic Chemistry Frontiers*. 2023; 10(9): 2618-2625.

[5] Domergue J, Guinard P, Douillard M, Pécaut J, Hostachy S, Proux O, et al. A series of Ni complexes based on a versatile ATCUN-like tripeptide scaffold to decipher key parameters for superoxide dismutase activity. *Inorganic Chemistry*. 2023; 62(23): 8747-8760.

[6] Sun X, Wang P, Yan X, Guo H, Wang L, Xu Q, et al. Hydride-doped $Ag_{17}Cu_{10}$ nanoclusters as high-performance electrocatalysts for CO_2 reduction. *Iscience*. 2023; 26(10): 107850. Available from: doi: 10.1016/j.isci.2023.107850.

[7] Pellegrini G, Mattei G, Bello V, Mazzoldi P. Interacting metal nanoparticles: Optical properties from nanoparticle dimers to core-satellite systems. *Materials Science and Engineering: C*. 2007; 27(5-8): 1347-1350.

[8] Barabás J, Vanbuel J, Ferrari P, Janssens E, Höltzl T. Non-covalent interactions and charge transfer between propene and neutral yttrium-doped and pure gold clusters. *Chemistry-A European Journal*. 2019; 25(69): 15795-15804.

[9] Bodiuzzaman M, Nag A, Narayanan RP, Chakraborty A, Bag R, Paramasivam G, et al. A covalently linked dimer of $[Ag_{25}(DMBT)_{18}]$. *Chemical Communications*. 2019; 55(34): 5025-5028.

[10] Chrétien S, Gordon MS, Metiu H. Binding of propene on small gold clusters and on Au (111): Simple rules for binding sites and relative binding energies. *The Journal of Chemical Physics*. 2004; 121(8): 3756-3766.

[11] Hofmann A, Schmiel P, Stein B, Graf C. Controlled formation of gold nanoparticle dimers using multivalent thiol ligands. *Langmuir*. 2011; 27(24): 15165-15175.

[12] Veerapandian M, Yun K. Functionalization of biomolecules on nanoparticles: specialized for antibacterial applications. *Applied Microbiology and Biotechnology*. 2011; 90: 1655-1667.

[13] Toshima N, Shiraishi Y, Teranishi T, Miyake M, Tominaga T, Watanabe H, et al. Various ligand-stabilized metal nanoclusters as homogeneous and heterogeneous catalysts in the liquid phase. *Applied Organometallic Chemistry*. 2001; 15(3): 178-196.

[14] Pandya A, Lad AN, Singh SP, Shanker R. DNA assembled metal nanoclusters: Synthesis to novel applications. *RSC Advances*. 2016; 6(114): 113095-113114.

[15] Shemetov AA, Nabiev I, Sukhanova A. Molecular interaction of proteins and peptides with nanoparticles. *ACS Nano*. 2012; 6(6): 4585-4602.

[16] Du X, Chai J, Yang S, Li Y, Higaki T, Li S, et al. Fusion growth patterns in atomically precise metal nanoclusters. *Nanoscale*. 2019; 11(41): 19158-19165.

[17] Jin R. Atomically precise metal nanoclusters: stable sizes and optical properties. *Nanoscale*. 2015; 7(5): 1549-1565.

[18] Yao Q, Wu Z, Liu Z, Lin Y, Yuan X, Xie J. Molecular reactivity of thiolate-protected noble metal nanoclusters: synthesis, self-assembly, and applications. *Chemical Science*. 2021; 12(1): 99-127.

[19] Takemura Y, Takenaka H, Nakajima T, Tanase, T. Hexa-and octagold chains from flexible tetragold molecular units supported by linear tetraphosphine ligands. *Angewandte Chemie International Edition*. 2009; 48(12): 2157-2161.
[20] Majzik A, Fülöp L, Csapó E, Bogár F, Martinek T, Penke B, et al. Functionalization of gold nanoparticles with amino acid, β-amyloid peptides and fragment. *Colloids and Surfaces B: Biointerfaces*. 2010; 81(1): 235-241.
[21] Govindachar DM, Periyasamy G. Influence of interface structure in redox and optical properties of thio and seleno-Ureidopeptide functionalized bimetallic gold nanocluster: DFT study. *Journal of Molecular Graphics and Modelling*. 2021; 106: 107929. Available from: doi: 10.1016/j.jmgm.2021.107929.
[22] Makrodimitris K, Masica DL, Kim ET, Gray JJ. Structure prediction of protein-solid surface interactions reveals a molecular recognition motif of statherin for hydroxyapatite. *Journal of the American Chemical Society*. 2007; 129(44): 13713-13722.
[23] Liu X, Saranya G, Huang X, Cheng X, Wang R, Chen M, et al. $Ag_2Au_{50}(PET)_{36}$ nanocluster: Dimeric assembly of $Au_{25}(PET)_{18}$ enabled by silver atoms. *Angewandte Chemie International Edition*. 2020; 59(33): 13941-13946.
[24] Hirano K, Takano S, Tsukuda T. Ligand effects on the structures of $[Au_{23}L_6(C \equiv CPh)_9]^{2+}$ (L = N-Heterocyclic Carbene vs Phosphine) with Au_{17} superatomic cores. *The Journal of Physical Chemistry C*. 2021; 125(18): 9930-9936.
[25] Zeng Y, Havenridge S, Gharib M, Baksi A, Weerawardene KDM, Ziefuß AR, et al. Impact of ligands on structural and optical properties of Ag_{29} nanoclusters. *Journal of the American Chemical Society*. 2021; 143(25): 9405-9414.
[26] Acres RG, Feyer V, Tsud N, Carlino E, Prince KC. Mechanisms of aggregation of cysteine functionalized gold nanoparticles. *The Journal of Physical Chemistry C*. 2014; 118(19): 10481-10487.
[27] Nieto-Ortega B, Burgi T. Vibrational properties of thiolate-protected gold nanoclusters. *Accounts of Chemical Research*. 2018; 51(11): 2811-2819.
[28] Periyasamy G, Durgun E, Raty JY, Remacle F. DFT studies of solvation effects on the nanosize bare, thiolated, and redox active ligated Au_{55} cluster. *The Journal of Physical Chemistry C*. 2010; 114(38): 15941-15950.
[29] Nair RV, Nair LV, Govindachar DM, Santhakumar H, Nazeer SS, Rekha CR, et al. Luminescent gold nanorods to enhance the near-infrared emission of a photosensitizer for targeted cancer imaging and dual therapy: Experimental and theoretical approach. *Chemistry-A European Journal*. 2020; 26(13): 2826-2836.
[30] Pillegowda M, Periyasamy G. DFT studies on the influence of ligation on optical and redox properties of bimetallic $[Au_4M_2]$ clusters. *RSC Advances*. 2016; 6(89): 86051-86060.
[31] Ni W, Mosquera RA, Pérez-Juste J, Liz-Marzán LM. Evidence for hydrogen-bonding-directed assembly of gold nanorods in aqueous solution. *The Journal of Physical Chemistry Letters*. 2010; 1(8): 1181-1185.
[32] Macfarlane RJ. From nano to macro: thinking bigger in nanoparticle assembly. *Nano Letters*. 2021; 21(18): 7432-7434.
[33] Tzeng BC, Yeh HT, Huang YC, Chao HY, Lee GH, Peng SM. A luminescent supermolecule with gold (I) quinoline-8-thiolate: crystal structure, spectroscopic and photophysical properties. *Inorganic Chemistry*. 2003; 42(19): 6008-6014.
[34] Pei Y, Tang J, Tang X, Huang Y, Zeng XC. New structure model of $Au_{22}(SR)_{18}$: Bitetrahederon golden kernel enclosed by $[Au_6(SR)_6]$ Au (I) complex. *The Journal of Physical Chemistry Letters*. 2015; 6(8): 1390-1395.
[35] An K, Somorjai GA. Size and shape control of metal nanoparticles for reaction selectivity in catalysis. *ChemCatChem*. 2012; 4(10): 1512-1524.
[36] Nassereddine A, Abdelrahman A, Benard E, Bedu F, Ozerov I, Limozin L, et al. Ligand nanocluster array enables artificial-intelligence-based detection of hidden features in T-cell architecture. *Nano Letters*. 2021; 21(13): 5606-5613.
[37] Lewis DJ, Pikramenou Z. Lanthanide-coated gold nanoparticles for biomedical applications. *Coordination Chemistry Reviews*. 2014; 273: 213-225.
[38] Mammen N, Narasimhan S, de Gironcoli S. Tuning the morphology of gold clusters by substrate doping. *Journal of the American Chemical Society*. 2011, 133(9): 2801-2803.
[39] De M, Ghosh PS, Rotello VM. Applications of nanoparticles in biology. *Advanced Materials*. 2008; 20(22): 4225-4241.
[40] Erathodiyil N, Ying JY. Functionalization of inorganic nanoparticles for bioimaging applications. *Accounts of Chemical Research*. 2011; 44(10): 925-935.
[41] Zong J, Cobb SL, Cameron NR. Peptide-functionalized gold nanoparticles: versatile biomaterials for diagnostic and therapeutic applications. *Biomaterials Science*. 2017; 5(5): 872-886.
[42] Schmid G. The relevance of shape and size of Au_{55} clusters. *Chemical Society Reviews*. 2008; 37(9): 1909-1930.
[43] Deska R, Obstarczyk P, Matczyszyn K, Olesiak-Bańska J. Circular dichroism of gold bipyramid dimers. *The*

Journal of Physical Chemistry Letters. 2021; 12(21): 5208-5213.
[44] Chan MS, Landig R, Choi J, Zhou H, Liao X, Lukin MD, et al. Stepwise ligand-induced self-assembly for facile fabrication of nanodiamond-gold nanoparticle dimers via noncovalent biotin-streptavidin interactions. *Nano Letters*. 2019; 19(3): 2020-2026.
[45] Chevrier DM, Chatt A, Zhang P. Properties and applications of protein-stabilized fluorescent gold nanoclusters: short review. *Journal of Nanophotonics*. 2012; 6(1): 064504. Available from: doi: 10.1117/1.JNP.6.064504.
[46] Sardar R, Heap TB, Shumaker-Parry JS. Versatile solid phase synthesis of gold nanoparticle dimers using an asymmetric functionalization approach. *Journal of the American Chemical Society*. 2007; 129(17): 5356-5357.
[47] Xue Y, Li X, Li H, Zhang W. Quantifying thiol-gold interactions towards the efficient strength control. *Nature Communications*. 2014; 5(1): 4348. Available from: doi: 10.1038/ncomms5348.
[48] Kryachko ES, Remacle F. Complexes of DNA bases and gold clusters Au_3 and Au_4 involving nonconventional N-H...Au hydrogen bonding. *Nano Letters*. 2005; 5(4): 735-739.
[49] Yuan X, Malola S, Deng G, Chen F, Hakkinen H, Teo BK, et al. Atomically precise alkynyl-and halide-protected AuAg nanoclusters $Au_{78}Ag_{66}(C \equiv CPh)_{48}C_{l8}$ and $Au_{74}Ag_{60}(C \equiv CPh)_{40}Br_{12}$: The ligation effects of halides. *Inorganic Chemistry*. 2021; 60(6): 3529-3533.
[50] Pan QJ, Zhang HX. Aurophilic attraction and excited-state properties of binuclear Au (I) complexes with bridging phosphine and/or thiolate ligands: An ab initio study. *The Journal of Chemical Physics*. 2003; 119(8): 4346-4352.
[51] Zhang S, Chandra KL, Gorman CB. Self-assembled monolayers of terminal alkynes on gold. *Journal of the American Chemical Society*. 2007; 129(16): 4876-4877.
[52] Qin Z, Sharma S, Wan CQ, Malola S, Xu WW, Häkkinen H, et al. A homoleptic alkynyl-ligated $[Au_{13}Ag_{16}L_{24}]^{3-}$ cluster as a catalytically active eight-electron superatom. *Angewandte Chemie International Edition*. 2021; 60(2): 970-975.
[53] Maity P, Takano S, Yamazoe S, Wakabayashi T, Tsukuda T. Binding motif of terminal alkynes on gold clusters. *Journal of the American Chemical Society*. 2013; 135(25): 9450-9457.
[54] Lei Z, Wan XK, Yuan SF, Wang JQ, Wang QM. Alkynyl-protected gold and gold-silver nanoclusters. *Dalton Transactions*. 2017; 46(11): 3427-3434.
[55] Mingos DMP. Gold-a flexible friend in cluster chemistry. *Journal of the Chemical Society, Dalton Transactions*. 1996; (5): 561-566.
[56] Surujpaul PP, Gutiérrez-Wing C, Ocampo-García B, Ramirez FDM, de Murphy CA, Pedraza-Lopez M, et al. Gold nanoparticles conjugated to $[Tyr_3]$ octreotide peptide. *Biophysical Chemistry*. 2008; 138(3): 83-90.
[57] Govindachar DM, Periyasamy G. DFT studies on ureido-peptide functionalized Au_4M_2 bimetallic nanoclusters. *Chemical Physics Letters*. 2020; 753: 137612. Available from: doi: 10.1016/j.cplett.2020.137612.
[58] Kurashige W, Yamaguchi M, Nobusada K, Negishi Y. Ligand-induced stability of gold nanoclusters: thiolate versus selenolate. *The Journal of Physical Chemistry Letters*. 2012; 3(18): 2649-2652.
[59] Pillegowda M, Periyasamy G. DFT studies on interaction between bimetallic $[Au_2M]$ clusters and cellobiose. *Computational and Theoretical Chemistry*. 2018; 1129: 26-36.
[60] Periyasamy G, Remacle F. Ligand and solvation effects on the electronic properties of Au_{55} clusters: A density functional theory study. *Nano Letters*. 2009; 9(8): 3007-3011.
[61] Wendy DC, Piotr C, Christopher IB, Ian RG, Kenneth MM, David MF, et al. A second generation force field for the simulation of proteins, nucleic acids, and organic molecules. *Journal of the American Chemical Society*. 1995; 117(19): 5179-5197.
[62] Ding S, Tian Y, Jiang Z, He X. Molecular dynamics simulation of joining process of Ag-Au nanowires and mechanical properties of the hybrid nanojoint. *AIP Advances*. 2015; 5(5): 057120. Available from: doi: 10.1063/1.4921075.
[63] Hess B, Kutzner C, Van Der Spoel D, Lindahl E. GROMACS 4: algorithms for highly efficient, load-balanced, and scalable molecular simulation. *Journal of Chemical Theory and Computation*. 2008; 4(3): 435-447.
[64] Frisch M. Gaussian. 2009. Available from: http://www. gaussian.com/ [Accessed 1st August 2023].
[65] Khondaker SI, Luo K, Yao Z. The fabrication of single-electron transistors using dielectrophoretic trapping of individual gold nanoparticles. *Nanotechnology*. 2010; 21(9): 095204. Available from: doi: 10.1088/0957-4484/21/9/095204.

Appendix

Method and software

The ligated dimeric metal clusters were considered with $[Au_6L]_2$ configurations for the present study. The AMBER99 force-fields are used to model ligands/solvents and the neutral metal atoms are modeled as Lennard-Jones (LJ) particles. The LJ parameters are taken from literature for gold atoms. These parameters are already used to study the interaction between ligand and metal clusters, which shows the reliability of the parameters. The transferable intermolecular potential three point (TIP3P) model is considered for water solvent. The MD simulation is performed using the GROMACS-5.1.1 MD package in an initial cubic water box of length 10 Å at room temperature (298 K) and constant atmospheric pressure (1 atm). Initially, the high energy contacts between the monomers in the initial conformations are removed by minimizing the energy using the steepest descent method. Following that, NPT and NVT simulations are carried out using a leap-frog algorithm for integrating Newton's equation of motion for 1.0 ns at constant temperature and pressure. The periodic boundary condition is applied in all three directions. Electrostatic interactions are calculated with the Particle Mesh Ewald (PME) method. The time step for the MD simulation is 1.5 fs. Atomic coordinates are recorded for every 7.5 ps for trajectory analysis.

DFT calculations are carried out with CAM-B3LYP long-range, wB97XD, and M06-HF dispersion corrected functional, LANL2DZ pseudopotential for Au, and 6-31 + G(d) basis set for all other atoms. Natural charges have been calculated using Natural charge analysis to check the charge distribution in the dimer. All the geometries were considered the lowest energy by performing a scan along with the coordinates method. The basis set superposition error (BSSE) in interaction energy value is attuned using the Boys and Bernardi counterpoise correction method as set in Gaussian 09 package. Time-dependent density functional theory has been calculated using the same level of theory for all the aggregations.

Table S1. Computed dipole moment for singlet states of all three orientations of all the ligated dimeric clusters at CAM-B3LYP level theory

Au_6-dimer	dipole moment (Debye)		
	Orientation I	Orientation II	Orientation III
$[Au_6]_2$	0.537	-	-
$[Au_6H]_2$	0.125	2.590	0.295
$[Au_6CH_3]_2$	0.053	4.615	0.435
$[Au_6C_2H_5]_2$	1.574	13.536	1.364
$[Au_6C_5H_9]_2$	1.512	16.265	1.601
$[Au_6C_6H_{11}]_2$	0.485	11.829	0.491
$[Au_6C_6H_5]_2$	0.684	1.315	0.395
$[Au_6C_6H_4CH_3]_2$	0.568	7.714	0.269
$[Au_6C_2H]_2$	1.360	5.184	2.558
$[Au_6C_2CH_3]_2$	1.198	2.306	1.201
$[Au_6C_2C_6H_5]_2$	1.207	8.211	1.609

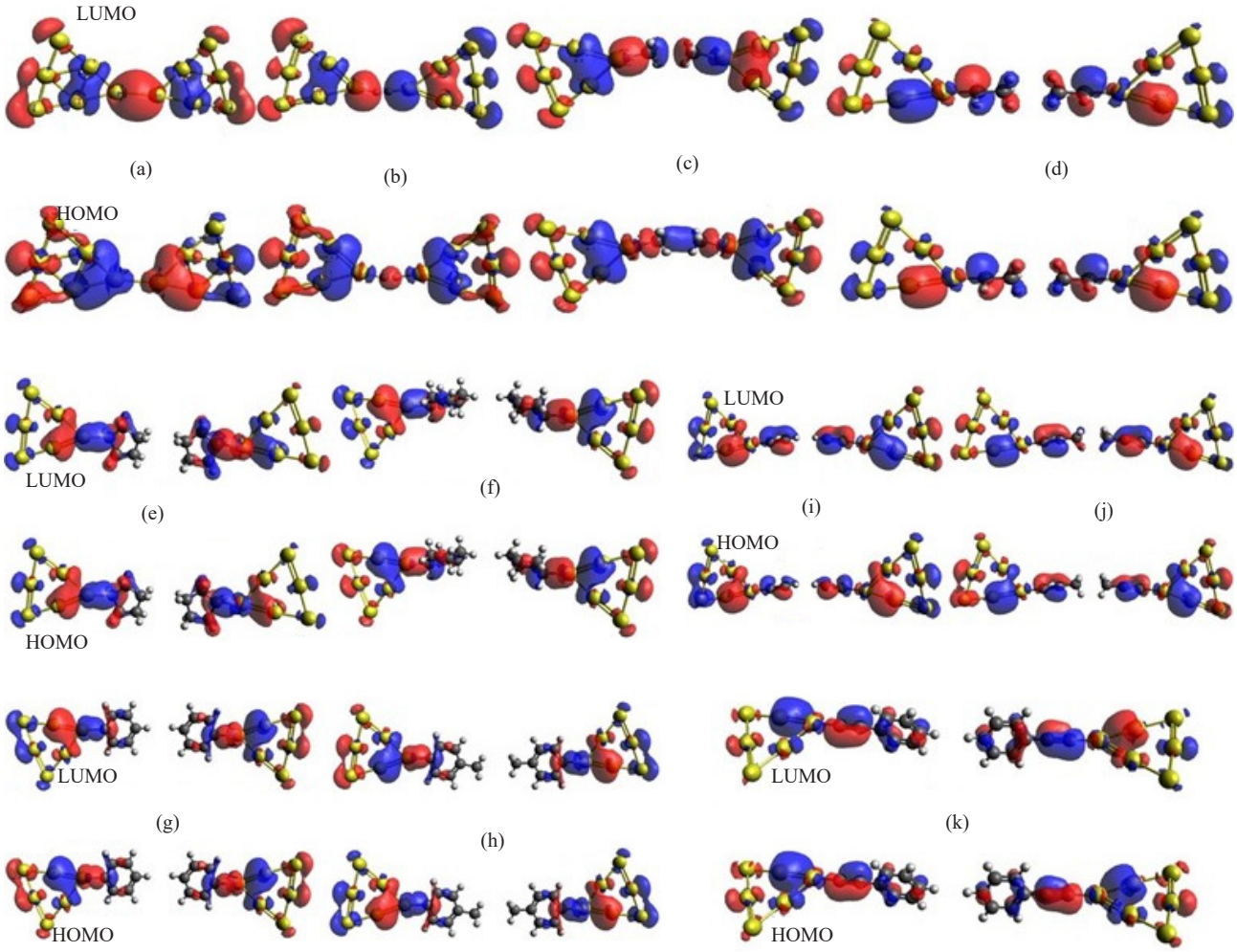

Figure S1. Orbital plots of all the dimers in orientation I studied with CAM-B3LYP functional, plotted with an isocontour value of 0.02 $Å^{-3}$. (a) $[Au_6]$ and orientation 1 of (b) $[Au_6H]_2$, (c) $[Au_6CH_3]_2$, (d) $[Au_6C_2H_5]_2$, (e) $[Au_6C_5H_9]_2$, (f) $[Au_6C_6H_{11}]_2$, (g) $[Au_6C_6H_5]_2$ and (h) $[Au_6C_6H_4CH_3]_2$, (i) $[Au_6C_2H]_2$, (j) $[Au_6C_2CH_3]_2$, and (k) $[Au_6C_2C_6H_5]_2$

Table S2. Computed $E_{(HOMO)}$, $E_{(LUMO)}$, Δ(HOMO-LUMO) in eV for dimeric models at the CAM-B3LYP functional

Dimer	$E_{(HOMO)}$	$E_{(LUMO)}$	Δ (eV)
$[Au_6]_2$	-7.97	-2.337	5.633
$[Au_6H]_2$	-7.409	-2.448	4.961
$[Au_6CH_3]_2$	-7.068	-2.284	4.784
$[Au_6C_2H_5]_2$	-7.222	-1.970	5.252
$[Au_6C_5H_9]_2$	-6.887	-1.972	4.915
$[Au_6C_6H_{11}]_2$	-6.735	-2.083	4.652
$[Au_6C_6H_5]_2$	-7.182	-2.306	4.876
$[Au_6C_6H_4CH_3]_2$	-7.132	-2.271	4.861
$[Au_6C_2H]_2$	-7.458	-2.269	5.189
$[Au_6C_2CH_3]_2$	-7.354	-2.256	5.098
$[Au_6C_2C_6H_5]_2$	-7.050	-2.102	4.948

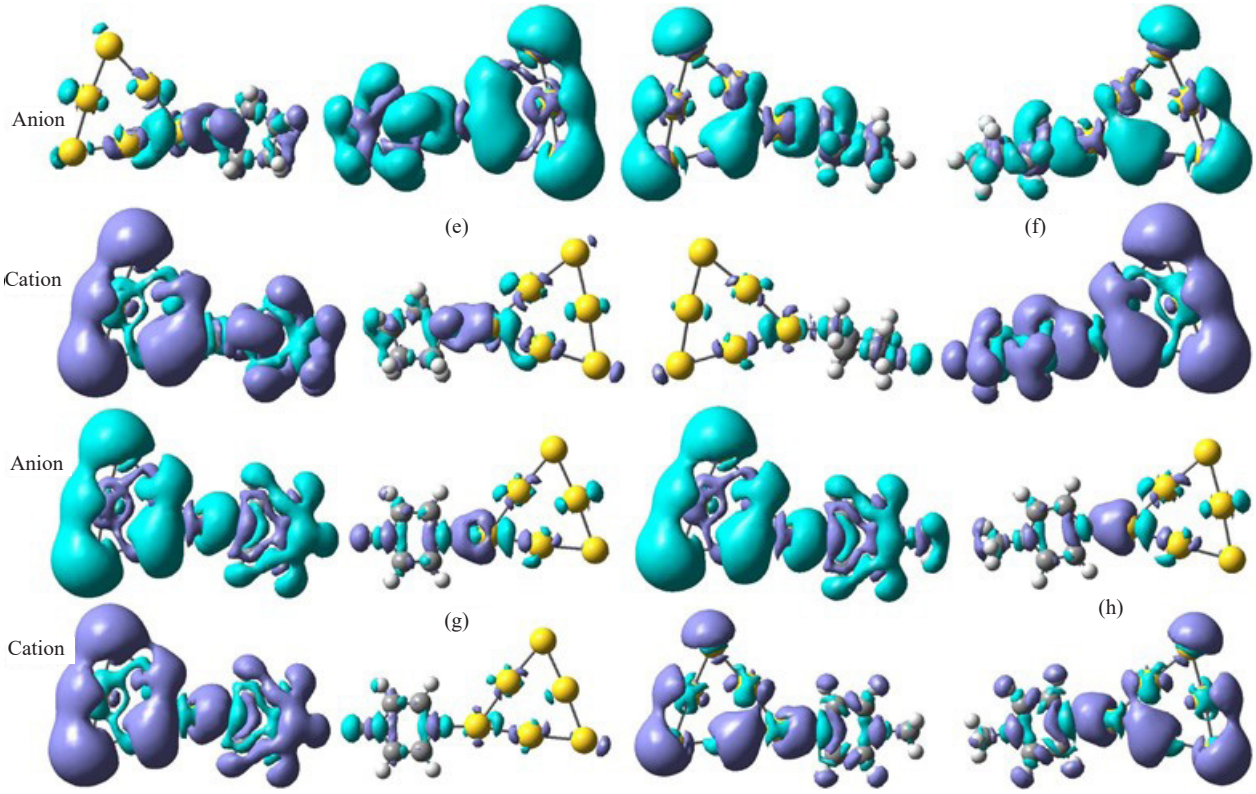

Figure S2. Computed plots of electron density difference between the neutral and charged clusters, where (e) $[Au_6C_5H_9]_2$, (f) $[Au_6C_6H_{11}]_2$, (g) $[Au_6C_6H_5]_2$ and (h) $[Au_6C_6H_4CH_3]_2$, plotted with a contour value of 0.02 $Å^{-3}$

Table S3. Computed $E_{(HOMO)}$, $E_{(LUMO)}$, $\Delta_{(HOMO-LUMO)}$, VEA, and VIP in eV at CAM-B3LYP, wB97XD, and M06-HF functional for all the ligated dimeric clusters

Models		$E_{(HOMO)}$	$E_{(LUMO)}$	Δ (eV)	VEA	VIP
$[Au_6]_2$	CAMB3LYP PCM	-7.515/ -6.936	-3.305/ -2.553	4.21/ 4.38	-3.025	-7.786
	wB97XD	-7.938	-2.701	5.237	-2.905	-7.714
	M06HF	-8.806	-2.306	6.50	-3.102	-7.726
$[Au_6H]_2$	CAMB3LYP PCM	-7.389/ -7.260	-3.032/ -1.893	4.357/ 4.367	-2.731	-7.636
	wB97XD	-7.817	-2.427	5.39	-2.638	-7.594
	M06HF	-8.716	-2.189	6.527	-2.818	-7.684
$[Au_6CH_3]_2$	CAMB3LYP PCM	-6.134/ -5.805	-4.565/ -3.736	1.569/ 2.069	-4.297	-6.411
	wB97XD	-6.398	-4.152	2.246	-4.324	-6.221
	M06HF	-6.664	-4.267	2.397	-4.798	-5.839
$[Au_6C_2H_5]_2$	CAMB3LYP PCM	-5.964/ -5.78	-4.959/ -4.054	1.005/ 1.726	-4.847	-6.074
	wB97XD	-6.186	-4.644	1.542	-4.907	-5.555
	M06HF	-6.401	-4.869	1.532	-5.769	-5.480

	CAMB3LYP PCM	-5.434/ -5.429	-4.647/ -3.844	0.787/ 1.585	-4.705	-5.652
$[Au_6C_5H_9]_2$	wB97XD	-5.589	-4.373	1.216	-4.606	-5.129
	M06HF	-5.85	-4.616	1.234	-5.394	-4.854
	CAMB3LYP PCM	-5.36/ -5.498	-4.723/ -3.674	0.637/ 1.824	-4.500	-5.671
$[Au_6C_6H_{11}]_2$	wB97XD	-5.46	-4.473	0.987	-4.725	-5.223
	M06HF	-5.644	-4.668	0.976	-5.576	-4.753
	CAMB3LYP PCM	-5.757/ -5.954	-5.179/ -3.899	0.578/ 2.055	-4.895	-6.064
$[Au_6C_6H_5]_2$	wB97XD	-5.841	-4.945	0.896	-5.205	-5.611
	M06HF	-6.055	-5.183	0.872	-6.171	-5.087
	CAMB3LYP PCM	-5.669/ -5.929	-5.167/ -3.901	0.502/ 2.028	-4.902	-5.888
$[Au_6C_6H_4CH_3]_2$	wB97XD	-5.732	-4.955	0.777	-5.211	-5.499
	M06HF	-5.952	-5.192	0.76	-6.188	-4.996

(1) $[Au_6]_2$

Au	-0.64035969	2.74691165	0.79701086
Au	-1.33586728	0.20929036	0.28786773
Au	1.38431106	1.09976250	0.18683300
Au	-1.82397304	-2.36962963	-0.25445769
Au	0.75149490	-1.63728369	-0.37539816
Au	3.26326701	-0.70483964	-0.44271962
Au	9.30123397	3.52038666	-0.22571200
Au	7.59720657	1.45447427	-0.32951928
Au	10.43190640	1.11221198	-0.55279544
Au	6.06301177	-0.73935674	-0.45814363
Au	8.69997967	-1.16660614	-0.67689120
Au	11.36424067	-1.37985074	-0.87493978

(2) $[Au_6H]_2$

Au	-3.85977369	1.20175970	-0.08147238
Au	-3.98518739	-1.46244957	-0.34365499
Au	-1.49599899	-0.04783658	-0.27064768
Au	-3.89663016	-4.12766197	-0.61196982
Au	-1.51540809	-2.89866585	-0.55415735
Au	0.75863555	-1.48254713	-0.47468096
Au	8.00161518	3.47728012	-0.26435357
Au	6.29758778	1.41136773	-0.36816085
Au	9.13228761	1.06910544	-0.59143701
Au	4.76339298	-0.78246328	-0.49678520
Au	7.40036088	-1.20971268	-0.71553277
Au	10.06462188	-1.42295728	-0.91358135
H	3.25355820	-1.42194352	-0.46416658

H	2.39800189	-1.48926231	-0.51976864

(3) $[Au_6CH_3]_2$

Au	-3.88914833	1.19735088	-0.08567868
Au	-4.01456203	-1.46685839	-0.34786129
Au	-1.52537363	-0.05224540	-0.27485398
Au	-3.92600480	-4.13207079	-0.61617612
Au	-1.54478273	-2.90307467	-0.55836365
Au	0.72926091	-1.48695595	-0.47888726
Au	10.48722109	4.21244602	-0.54866527
Au	8.88411136	2.07019620	-0.39607362
Au	11.73569163	1.84058412	-0.53130328
Au	7.45710096	-0.19365563	-0.24839608
Au	10.11508684	-0.51647724	-0.37041871
Au	12.78990255	-0.62337415	-0.50048463
H	3.12437237	-1.84270286	0.33258378
H	3.07898212	-2.08316803	-1.28196968
H	3.10167724	-0.56415067	-0.68302239
H	5.65918169	-1.84564202	0.49995362
H	4.95382379	-0.40123441	0.21216281
H	5.33882023	-1.38451324	-1.03347243
C	5.61781256	-1.06765317	-0.12696100
C	2.76847270	-1.49530898	-0.53497194

(4) $[Au_6C_2H_5]_2$

Au	-7.80334134	0.26153377	-1.16794740
Au	-7.92889495	-2.40215561	-1.43529457
Au	-5.43963174	-0.98781951	-1.35952581
Au	-7.84047764	-5.06684764	-1.70877421
Au	-5.45919052	-3.83809285	-1.64856089
Au	-3.18507204	-2.42225209	-1.56632183
Au	9.37883053	4.88126909	-1.40561436
Au	8.12443559	2.51376665	-1.46810302
Au	10.97922481	2.73467931	-1.53051221
Au	7.06291943	0.05382461	-1.53924415
Au	9.74067948	0.15225504	-1.60173280
Au	12.40175550	0.46658186	-1.65517652
C	0.37264089	-1.61824192	-1.43711178
C	-1.12349316	-1.97780930	-1.49951528
H	-0.96143892	-2.79745866	-0.83107429
C	5.01137835	-0.43189993	-1.45350688
H	5.15603704	-0.87269699	-0.48931197
C	3.51404350	-0.78640263	-1.39092759
H	2.93801599	0.02938362	-1.77509565
H	0.80628445	-2.04756644	-0.55817280
H	3.23400192	-0.97369754	-0.37535025
H	0.48278857	-0.55438117	-1.40600230
H	0.86837136	-2.00294886	-2.30380196

H	3.32975654	-1.66120431	-1.97885646
H	5.11575799	-1.02847860	-2.33560595
H	-1.04518918	-2.15020117	-2.55262949

(5) $[Au_6C_5H_9]_2$

Au	-3.47368067	-2.81918363	-0.16314633
Au	-1.14671918	-1.15998239	-0.34974830
Au	-3.17365257	-5.44276968	-0.62137301
Au	-0.93762554	-3.97830712	-0.82018157
Au	1.17837496	-2.34026397	-0.96964626
Au	15.99868905	5.52258393	-1.67406099
Au	14.74450768	3.15486853	-1.73264578
Au	17.59930716	3.37588927	-1.79419726
Au	13.68321618	0.69471266	-1.79962267
Au	16.36099614	0.79323721	-1.86110170
Au	19.02207111	1.10767350	-1.91395030
C	3.16352835	-1.80609296	-1.44496444
C	4.10409839	-0.66287232	-1.09222326
C	4.00987912	-2.98675137	-1.89958681
H	2.45933920	-1.49539031	-2.25735072
C	5.52226382	-1.10257383	-1.42618524
H	4.02055770	-0.41240002	-0.00455360
H	3.83350962	0.25981144	-1.66395893
C	5.47048908	-2.56058523	-1.85970266
H	3.72115335	-3.29821457	-2.93487481
H	3.84203496	-3.86897154	-1.23209754
H	5.94327881	-0.46784610	-2.24624976
H	6.19179974	-0.97956800	-0.53846549
H	5.94421746	-2.68755664	-2.86529469
H	6.04336100	-3.20104618	-1.14275032
C	11.63957553	0.19213432	-1.64780725
C	11.44262900	-1.29538063	-1.90189991
C	10.27891488	0.79907754	-1.33608951
H	12.08987473	0.68505369	-2.54594482
C	9.94984068	-1.58651067	-1.84816429
H	11.98421422	-1.89675449	-1.12874038
H	11.86393328	-1.58357276	-2.89733615
C	9.23813120	-0.30739882	-1.43132171
H	10.04357046	1.62100216	-2.05806323
H	10.27668879	1.25034170	-0.31218437
H	9.58362968	-1.92652060	-2.84962397
H	9.73541705	-2.41047236	-1.12251646
H	12.08987473	0.68505369	-2.54594482
C	9.94984068	-1.58651067	-1.84816429
H	11.98421422	-1.89675449	-1.12874038
H	11.86393328	-1.58357276	-2.89733615
C	9.23813120	-0.30739882	-1.43132171
H	10.04357046	1.62100216	-2.05806323
H	10.27668879	1.25034170	-0.31218437

H	9.58362968	-1.92652060	-2.84962397
H	9.73541705	-2.41047236	-1.12251646
H	8.44660727	-0.03904761	-2.17511813
H	8.72865919	-0.44845840	-0.44494775

(6) $[Au_6C_6H_{11}]_2$

Au	-8.28224349	0.16056759	-1.15193805
Au	-8.40774380	-2.50261826	-1.42428000
Au	-5.91853613	-1.08827446	-1.34684838
Au	-8.31927564	-5.16678192	-1.70284369
Au	-5.93803909	-3.93799630	-1.64127498
Au	-3.66397359	-2.52217339	-1.55728236
Au	12.40212399	4.63362588	-1.79928370
Au	11.14794262	2.26591048	-1.85786850
Au	14.00274209	2.48693122	-1.91941998
Au	10.08665111	-0.19424539	-1.92484539
Au	12.76443107	-0.09572084	-1.98632442
Au	15.42550604	0.21871545	-2.03917302
C	-1.60239471	-2.07773060	-1.49047581
C	-0.94029318	-2.90042207	-0.40393577
C	-0.97926341	-2.35291595	-2.84418315
H	-1.50001149	-0.98746459	-1.24756212
C	0.55754526	-2.67408813	-0.37566635
H	-1.14942201	-3.98824099	-0.58079445
H	-1.37948393	-2.63052846	0.59150438
C	0.51847769	-2.12578721	-2.81610141
H	-1.19021347	-3.41334725	-3.14306843
H	-1.44580777	-1.68625793	-3.61512085
C	1.18123742	-2.94708051	-1.72905588
H	1.02386506	-3.34199701	0.39435247
H	0.76869900	-1.61421644	-0.07489277
H	0.95775540	-2.39610691	-3.81134422
H	0.72687070	-1.03763152	-2.64014772
H	2.27596764	-2.70863201	-1.69294629
H	1.08154258	-4.03759177	-1.97235005
C	8.04120974	-0.71120419	-1.95683302
C	7.47215812	-1.28365719	-3.23911488
C	7.62601785	-1.53634003	-0.75545478
H	7.68155794	0.34331718	-1.82720043
C	5.96532533	-1.42121493	-3.16114682
H	7.92860821	-2.28994274	-3.43252265
H	7.74431695	-0.61929691	-4.10003714
C	6.11912504	-1.67320273	-0.67705117
H	8.09003599	-2.55528299	-0.82465947
H	8.00861980	-1.05467238	0.18159032
C	5.54908170	-2.24436728	-1.95933926
H	5.58330166	-1.90426787	-4.09773808
H	5.50104909	-0.40224252	-3.09390500
H	5.84695529	-2.33791350	0.18354694

H	5.66340366	-0.66671716	-0.48269323
H	4.43042846	-2.27290637	-1.89303464
H	5.90621200	-3.29986988	-2.08863789

(7) $[Au_6C_6H_5]_2$

Au	-8.02650137	0.20621465	-1.16991607
Au	-8.15205498	-2.45747473	-1.43726324
Au	-5.66279177	-1.04313863	-1.36149448
Au	-8.06363767	-5.12216676	-1.71074288
Au	-5.68235055	-3.89341197	-1.65052956
Au	-3.40823207	-2.47757121	-1.56829050
Au	12.87133100	4.81101130	-1.74267909
Au	11.61693606	2.44350886	-1.80516775
Au	14.47172528	2.66442152	-1.86757694
Au	10.55541990	-0.01643318	-1.87630888
Au	13.23317995	0.08199725	-1.93879753
Au	15.89425597	0.39632407	-1.99224125
C	-1.34665319	-2.03312842	-1.50148395
C	-0.62329496	-3.22144408	-1.60698374
C	-0.67919166	-0.80837106	-1.49793035
C	0.76725893	-3.18494517	-1.70822326
H	-1.14974732	-4.18688994	-1.60898184
C	0.71170913	-0.77164480	-1.60018525
H	-1.24916829	0.12831069	-1.41496673
C	1.43499541	-1.95965528	-1.70518560
H	1.33753247	-4.12157412	-1.79075086
H	1.23767218	0.19418711	-1.59777073
C	8.50387882	-0.50215772	-1.79057161
C	7.54636638	0.51026789	-1.85865773
C	8.10400387	-1.83640344	-1.71683878
C	6.18930105	0.18846773	-1.85232602
H	7.86193725	1.56210836	-1.91600255
C	6.74657357	-2.15852801	-1.71148920
H	8.85854181	-2.63448893	-1.66334986
C	5.78922990	-1.14637098	-1.77907820
H	5.43451551	0.98645460	-1.90535666
H	6.43158948	-3.21063384	-1.65376080
H	2.50180664	-1.93189435	-1.78292312
H	4.74805632	-1.39301782	-1.77429227

(8) $[Au_6C_6H_4CH_3]_2$

Au	-8.07025948	0.19571706	-1.17008421
Au	-8.19581309	-2.46797232	-1.43743138
Au	-5.70654988	-1.05363622	-1.36166262
Au	-8.10739578	-5.13266435	-1.71091102
Au	-5.72610866	-3.90390956	-1.65069770
Au	-3.45199018	-2.48806880	-1.56845864
Au	15.03886744	5.48001577	-1.67596794

Au	13.78447250	3.11251333	-1.73845660
Au	16.63926172	3.33342599	-1.80086579
Au	12.72295634	0.65257129	-1.80959773
Au	15.40071639	0.75100172	-1.87208638
Au	18.06179241	1.06532854	-1.92553010
C	-1.39041130	-2.04362601	-1.50165209
C	-0.66705307	-3.23194167	-1.60715188
C	-0.72294977	-0.81886865	-1.49809849
C	0.72350082	-3.19544276	-1.70839140
H	-1.19350543	-4.19738753	-1.60914998
C	0.66795102	-0.78214239	-1.60035339
H	-1.29292640	0.11781310	-1.41513487
C	1.39123730	-1.97015287	-1.70535374
H	1.29377436	-4.13207171	-1.79091900
H	1.19391407	0.18368952	-1.59793887
C	10.67141526	0.16684675	-1.72386046
C	9.71390282	1.17927236	-1.79194658
C	10.27154031	-1.16739897	-1.65012763
C	8.35683749	0.85747220	-1.78561487
H	10.02947369	2.23111283	-1.84929140
C	8.91411001	-1.48952354	-1.64477805
H	11.02607825	-1.96548446	-1.59663871
C	7.95676634	-0.47736651	-1.71236705
H	7.60205195	1.65545907	-1.83864551
H	8.59912592	-2.54162937	-1.58704965
C	2.92664786	-1.93019789	-1.81723764
H	3.34257796	-2.78335499	-1.32324865
H	3.20950805	-1.94244036	-2.84910015
H	3.29466837	-1.03703737	-1.35710159
C	6.45825483	-0.83235355	-1.70547889
H	6.02214584	-0.52071676	-0.77941655
H	5.96964751	-0.33279742	-2.51579152
H	6.34179800	-1.89019326	-1.81644268

(9) $[Au_6C_2H]_2$

Au	-8.35085798	2.73408585	0.67444811
Au	-8.97361623	0.17959841	0.15555951
Au	-6.28995092	1.16512811	-0.01529293
Au	-9.38876470	-2.40858629	-0.40313911
Au	-6.84481577	-1.58588716	-0.59150643
Au	-4.36977081	-0.56602822	-0.72198025
Au	10.13017858	3.70568449	-0.24846647
Au	8.42615118	1.63977210	-0.35227375
Au	11.26085101	1.29750981	-0.57554991
Au	6.89195638	-0.55405891	-0.48089810
Au	9.52892428	-0.98130831	-0.69964567
Au	12.19318528	-1.19455291	-0.89769425
C	-2.28385151	-0.34712126	-0.49150158
C	4.80027399	-0.35792309	-0.28469535

C	-0.76142716	-0.18734464	-0.32328886
C	3.27364249	-0.21477231	-0.14150274
H	0.29636055	-0.07632820	-0.20640981
H	2.21293124	-0.11530622	-0.04201358

(10) $[Au_6C_2CH_3]_2$

Au	-9.82827494	2.63820664	0.64061890
Au	-10.45103319	0.08371920	0.12173030
Au	-7.76736788	1.06924890	-0.04912214
Au	-10.86618166	-2.50446550	-0.43696832
Au	-8.32223273	-1.68176637	-0.62533564
Au	-5.84718777	-0.66190743	-0.75580946
Au	10.56743827	3.71488392	-0.21463726
Au	8.86341087	1.64897153	-0.31844454
Au	11.69811070	1.30670924	-0.54172070
Au	7.32921607	-0.54485948	-0.44706889
Au	9.96618397	-0.97210888	-0.66581646
Au	12.63044497	-1.18535348	-0.86386504
C	-3.76126847	-0.44300047	-0.52533079
C	5.23753368	-0.34872366	-0.25086614
C	-2.23884412	-0.28322385	-0.35711807
C	3.71090218	-0.20557288	-0.10767353
C	-0.71642082	-0.12344320	-0.18889964
H	-0.22103915	-0.98226009	-0.59130559
H	-0.39013322	0.75285210	-0.70903709
H	-0.48030293	-0.02990521	0.85052278
C	2.18427101	-0.06241608	0.03551648
H	1.81105843	0.57157909	-0.74144072
H	1.72692185	-1.02675658	-0.04050424
H	1.95412193	0.36739532	0.98798358

(11) $[Au_6C_2C_6H_5]_2$

Au	-12.43211250	2.78449881	0.44419315
Au	-13.05443465	0.23087876	-0.07946615
Au	-10.37101242	1.21730307	-0.24896842
Au	-13.46914792	-2.35631817	-0.64304171
Au	-10.92541113	-1.53272017	-0.83034289
Au	-8.45060837	-0.51208830	-0.95935889
Au	15.02516615	3.99313259	-0.14015861
Au	13.32149294	1.92671758	-0.23968713
Au	16.15621424	1.58453733	-0.46281643
Au	11.78767095	-0.26763293	-0.36381743
Au	14.42467648	-0.69482705	-0.58221911
Au	17.08894021	-0.90797205	-0.78033812
C	-6.36468907	-0.29318134	-0.72888025
C	9.69598856	-0.07149708	-0.16761466
C	-4.84226472	-0.13340471	-0.56066754
C	8.16935706	0.07165370	-0.02442204

C	-3.31984142	0.02637594	-0.39244911
C	-2.56318737	0.60993046	-1.40901696
C	-2.69738533	-0.41218151	0.77620992
C	-1.18429857	0.75424075	-1.25715538
H	-3.05411012	0.95487837	-2.33056326
C	-1.31822450	-0.26700394	0.92868537
H	-3.29362044	-0.87197395	1.57759849
C	-0.56162063	0.31596980	-0.08779346
H	-0.58774096	1.21362424	-2.05864296
H	-0.82777641	-0.61250617	1.85040284
H	0.52558897	0.42991217	0.03174218
C	6.64272589	0.21481050	0.11876797
C	6.05021862	0.13873222	1.37956877
C	5.85235839	0.42063550	-1.01194129
C	4.66757832	0.26778647	1.50946314
H	6.67352571	-0.02431211	2.27071781
C	4.46938407	0.55073420	-0.88207116
H	6.31920049	0.48080039	-2.00570568
C	3.87689985	0.47421130	0.37834294
H	4.20042087	0.20720487	2.50313828
H	0.52558897	0.42991217	0.03174218
C	6.64272589	0.21481050	0.11876797
C	6.05021862	0.13873222	1.37956877
H	3.84650936	0.71342193	-1.77371796
H	2.78676450	0.57599515	0.48101377